URSI GASS 2023, Sapporo, Japan, 19 – 26 August 2023

Calibration of Pi-SAR2 Polarimetric Observation Data Using ABCI

Yuya Arima(1)*, Toshifumi Moriyama(2), Yoshio Yamaguchi(3), Ryosuke Nakamura(1),
Chiaki Tsutsumi(1), and Shoichiro Kojima(4)
(1) National Institute of Advanced Industrial Science and Technology (AIST), Tokyo, Japan
(2) Nagasaki University, Nagasaki, Japan
(3) Niigata University, Niigata, Japan
(4) National Institute of Information and Communications Technology (NICT), Koganei, Japan
*Correspondence: y-arima@aist.go.jp

Abstract

The polarimetric observation data of Pi-SAR2, an airborne polarimetric synthetic aperture radar, are very valuable because of its high resolution, but it cannot be used effectively because the data are not well calibrated with respect to elevation. Therefore, we have calibrated the data according to the observation conditions. The Pi-SAR2 observation data are very large due to its high resolution and require sufficient computational resources to be calibrated. We utilized the AI Bridging Cloud Infrastructure (ABCI) to calculate them. This paper reports on the calibration and scattering power decomposition of the Pi-SAR2 observation data using the ABCI.

1 Introduction

The Digital Architecture Research Center of the National Institute of Advanced Industrial Science and Technology (AIST) conducts research using remote sensing data provided by various organizations. One of the remote sensing data provided is Pi-SAR2 observation data.

Pi-SAR2 is an X-band airborne polarimetric synthetic aperture radar (SAR) operated by the National Institute of Information and Communications Technology (NICT). Pi-SAR2 can observe full-polarimetric and interferometric data in a single flight by means of antennas in two antenna pods mounted on the bottom of the aircraft. The greatest advantage of Pi-SAR2 is its high resolution, with a spatial resolution of up to 0.3 m (both azimuth and slant range) [1]. The Pi-SAR2 observation data are very valuable because of its high resolution, but it cannot be used effectively because the data are not well calibrated with respect to elevation. The Pi-SAR2 observation data are very large due to its high resolution and require sufficient computational resources to perform calibration and other tasks. Therefore, we used the AI Bridging Cloud Infrastructure (ABCI) [2], one of the world's largest computational infrastructures operated by the AIST, to perform the elevation calibration.

In this study, we have calibrated the Pi-SAR2 observational data through two stages utilizing the ABCI. In addition, we have verified the calibration results by performing scattering power decomposition. Scattering power decomposition data is intuitively easy to understand visually and can be used for deep learning and other applications. In this paper, we report on the calibration and scattering power decomposition of the Pi-SAR2 observation data using the ABCI.

2 Elevation Correction

Pi-SAR2 uses separate antennas for H and V polarization observations. Therefore, a phase difference is observed due to the difference in path length between the target and the two antennas. Figure 1 shows a VV polarization image observed by the main antenna of Pi-SAR2. The brightness of each pixel indicates the amplitude of the signal, and the hue indicates the phase. Since the phase is normalized with respect to the HH polarization, the phase shown in this image represents the phase difference between the VV and HH polarizations. The phase rotation correlated with the elevation of mountains is seen in the image.

We use interferometric data between the main and sub antennas for correction [3]. Figure 2(a) shows a schematic diagram of the observation of the main and sub antennas. When R_M and R_S denote the distance between each antenna and Target 1 at an elevation H, R_S can be written as the following equation,

$$\begin{aligned} R_S &= \sqrt{(R_M\cos\theta_0 - B\sin\alpha)^2 + (R_M\sin\theta_0 + B\cos\alpha)^2} \\ &\simeq R_M + B\sin(\theta_0-\alpha) \quad (B \ll R_M) \end{aligned} \tag{1}$$

where B is the baseline length between the two antennas, α is the inclination of the aircraft, and θ_0 is the angle of incidence. Furthermore, when λ denotes the wavelength, the phase difference $\phi_M - \phi_S$ is written as the following equation,

$$\phi_M - \phi_S = -\frac{2\pi}{\lambda} B\sin(\theta_0-\alpha) \tag{2}$$

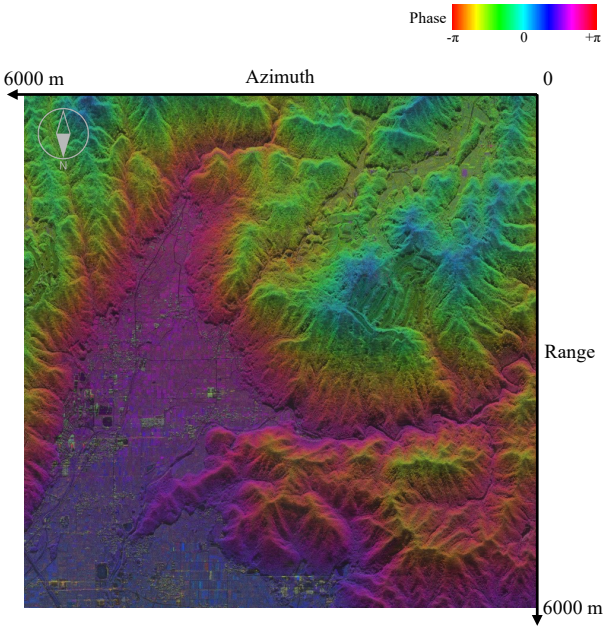

Figure 1. Original Pi-SAR2 VVm image at Kameoka on 16 October 2013. (Center: N34.987, E135.528).

When Target 2 is a point on the reference plane where the distance R_M from the main antenna is the same and the angle of incidence is θ_0', the following equation is similarly obtained.

$$\phi_M - \phi_S' = -\frac{2\pi}{\lambda} B \sin(\theta_0' - \alpha) \tag{3}$$

As a result, the interferometric phase difference after removing the flat earth phase $(\phi_M - \phi_S)_{\text{after flat earth}}$ is written as follows,

$$\begin{aligned}(\phi_M - \phi_S)_{\text{after flat earth}} &= -\frac{2\pi}{\lambda} B\{\sin(\theta_0 - \alpha) - \sin(\theta_0' - \alpha)\} \\ &\simeq -\frac{2\pi}{\lambda} B(\theta_0 - \theta_0')\cos(\theta_0' - \alpha)\end{aligned} \tag{4}$$

Where we approximated $\sin(\frac{\theta_0 - \theta_0'}{2}) \simeq \frac{\theta_0 - \theta_0'}{2}$ and $\frac{\theta_0 + \theta_0'}{2} \simeq \theta_0$ since $|\theta_0 - \theta_0'| \ll 1$. Figure 2(b) shows a schematic diagram of the observations with the H- and V-polarized antennas in the main antenna pod. The phase difference between the H- and V-polarized antennas after removing the flat earth phase $(\phi_V - \phi_H)_{\text{after flat earth}}$ is similarly written as follows,

$$(\phi_V - \phi_H)_{\text{after flat earth}} \simeq -\frac{2\pi}{\lambda} B_{pol}(\theta_0 - \theta_0')\cos(\theta_0' - \alpha_{pol}) \tag{5}$$

where B_{pol} is the distance between the centers of the H- and V-polarized antennas and α_0 is the inclination of the antennas. From Equations (4) and (5), the compensation formula is written as follows,

$$(\phi_V - \phi_H)_{\text{after flat earth}} = -\frac{B_{pol}\cos(\theta_0' - \alpha_{pol})}{B\cos(\theta_0' - \alpha)}(\phi_M - \phi_S)_{\text{after flat earth}} \tag{6}$$

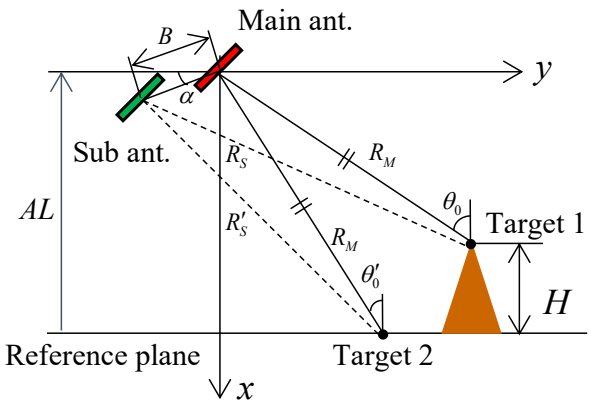

(a) Interferometric observation

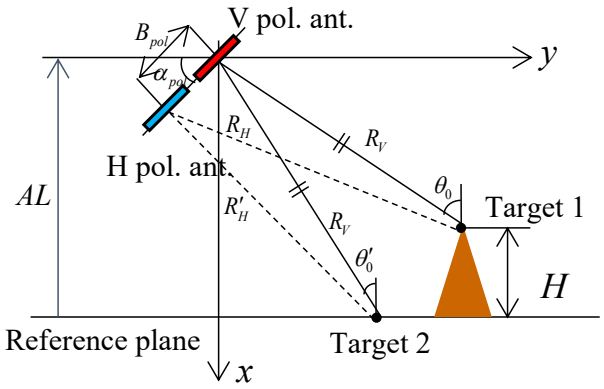

(b) Polarimetric observation

Figure 2. Observation geometric of Pi-SAR2.

Since this formula represents a one-way component, it is subtracted as is for HV and VH polarization and doubled and subtracted for VV polarization.

Figure 3 shows the result of elevation correction. The phase rotation correlated with elevation has been removed.

3 Polarimetric Calibration

We performed polarimetric calibration on the elevation-corrected data. When the measured scattering matrix after elevation correction is $\boldsymbol{Z}$ and the true scattering matrix is $\boldsymbol{S}$, the relation can be written as follows,

$$\begin{aligned}\boldsymbol{Z} &= A\boldsymbol{RST} + \boldsymbol{N} \\ &= A\begin{pmatrix}1 & \delta_1 \\ \delta_2 & f_1\end{pmatrix}\begin{pmatrix}S_{HH} & S_{HV} \\ S_{VH} & S_{VV}\end{pmatrix}\begin{pmatrix}1 & \delta_3 \\ \delta_4 & f_2\end{pmatrix} + \boldsymbol{N}\end{aligned} \tag{7}$$

where A is the gain, $\boldsymbol{R}$ and $\boldsymbol{T}$ are the error matrices in the receive/transmit system, $\boldsymbol{N}$ is the system noise, f_1 and f_2 are the H/V polarization imbalance of the receive/transmit system, and $\delta_1, \delta_2, \delta_3$ and δ_4 are cross-talk. We assume that the system noise $\boldsymbol{N}$ has already been sufficiently eliminated in the provided data and set $A = 1$ for the sake of simplicity. Since the crosstalk δ were very small, about -32 dB, we

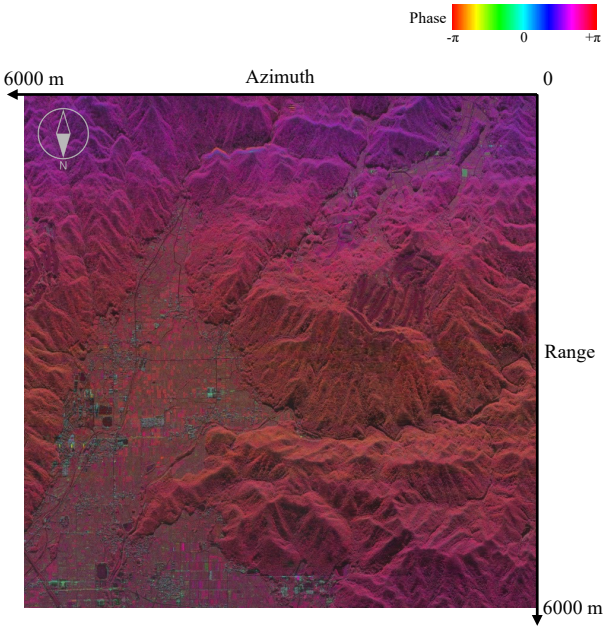

Figure 3. VVm image after elevation correction at Kameoka on 16 October 2013.

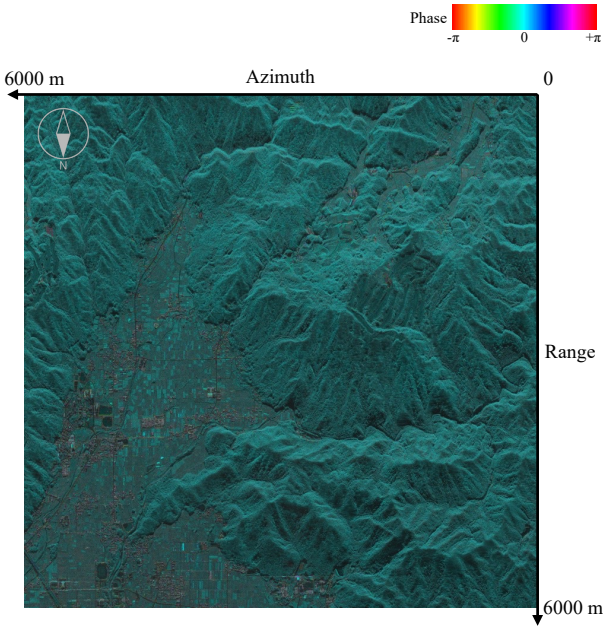

Figure 4. VVm image after polarimetric calibration at Kameoka on 16 October 2013.

considered them to be zero. When we define $\boldsymbol{S'}$ as the post-calibration scattering matrix to obtain, we calibrate it by using the following equation,

$$\boldsymbol{S'} = \boldsymbol{R}^{-1}\boldsymbol{Z}\boldsymbol{T}^{-1} = \begin{pmatrix} 1 & 0 \\ 0 & \frac{1}{f_1} \end{pmatrix} \begin{pmatrix} Z_{HH} & Z_{HV} \\ Z_{VH} & Z_{VV} \end{pmatrix} \begin{pmatrix} 1 & 0 \\ 0 & \frac{1}{f_2} \end{pmatrix}$$
$$\begin{cases} S'_{HH} = Z_{HH}, & S'_{HV} = \frac{1}{f_2} Z_{HV} \\ S'_{VH} = \frac{1}{f_1} Z_{VH}, & S'_{VV} = \frac{1}{f_1 f_2} Z_{VV} \end{cases} \tag{8}$$

There are two methods for estimating f_1 and f_2: one using corner reflectors (CRs) and the other using natural terrain. CRs were in place for some of the Pi-SAR2 observations, but not for the majority. Therefore, we estimate the imbalance by decomposing it into amplitude and phase. In other words, $|f_1|$ and $|f_2|$ are calculated from the observation data with CRs, while $Arg(f_1)$ and $Arg(f_2)$ are calculated from the individual observation data to be calibrated. This is because the amplitude of imbalance varies little from observation to observation, while the phase of imbalance is affected by the attachment and removal of the antenna to the aircraft for each observation.

In some observation series, CRs were placed on the beach near Niigata University. We obtained the calibration values from the ratio of the scattering intensities for each polarization at the CR positions for the four-observation data with CRs. The calculated ratio of scattering intensities VV/HH averaged 1.4045 with a minimum value of 1.3611 and a maximum value of 1.4873. Therefore, we set the imbalance amplitude $|f_1 f_2| = 1.4$. Since there was no significant difference in the scattering intensity at the CR positions between HV and VH polarizations, $|f_1| = |f_2| = \sqrt{1.4}$ are used.

The phase of imbalance $Arg(f_1 f_2)$ is calculated from the following equation derived from $Arg\langle S_{HH} S^*_{VV} \rangle = 0$ in natural terrain.

$$Arg(f_1 f_2) = Arg\langle Z_{HH} Z^*_{VV} \rangle \tag{9}$$

We set the averaging window size to 40 pixels and the slide size to 20 pixels. Furthermore, based on Quegan's method [4], $Arg(f_1/f_2)$ was calculated from the HV and VH polarization data according to the following equation,

$$Arg(f_1/f_2) = Arg\langle Z_{HV} Z^*_{VH} \rangle \tag{10}$$

We calculated $Arg(f_1/f_2)$ from the average over the entire scene.

Figure 4 shows the VV polarization image after calibration. Most of the image appears green, indicating phase of around 0, while buildings appear red, indicating phase of around π.

4 Scattering Power Decomposition

The calibrated observation data are processed by scattering power decomposition based on the scattering model. Scattering power decomposition has the advantage of being easy to understand because color correspond to the scattering mechanism. In deep learning, the scattering power decomposition data is input instead of the raw observation data may have the advantage of improving the performance, due to greater focus on the scattering mechanism. In addition, since the scattering power decomposition is not performed correctly with the insufficiently calibrated data, we used it as a benchmark to evaluate the calibration. There are several algorithms for scattering power decomposition. In

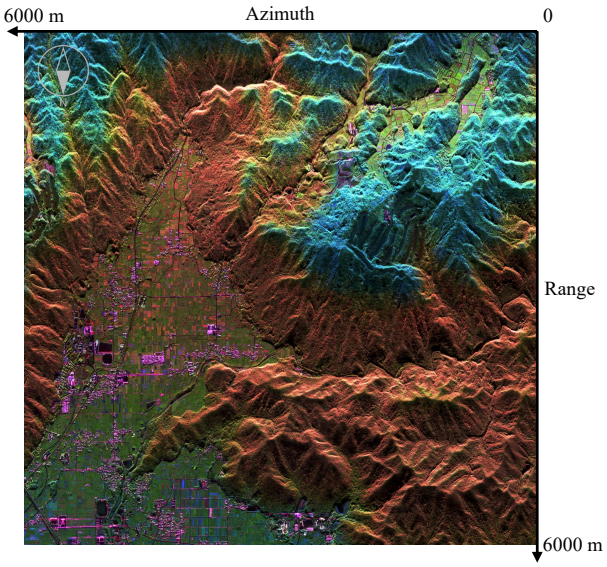

Figure 5. G4U image before calibration at Kameoka on 16 October 2013.

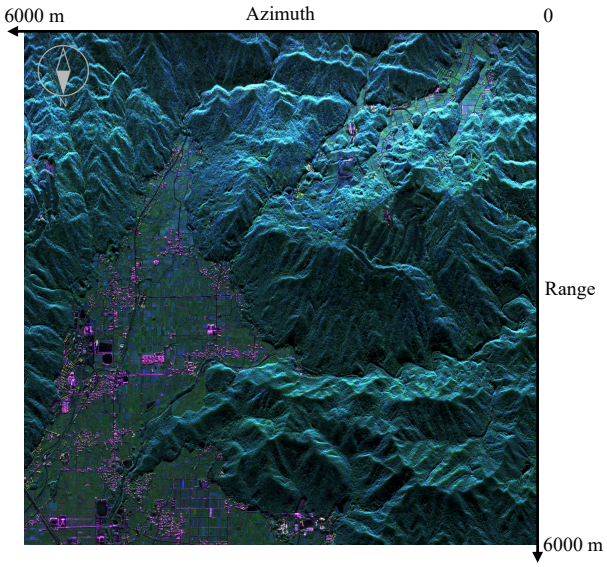

Figure 6. G4U image after calibration at Kameoka on 16 October 2013.

this paper we use two algorithms, G4U [5] . The G4U algorithm decomposes into four components: surface scattering P_s, double bounce scattering P_d, volume scattering P_v, and helix scattering P_c. It is known that P_v is dominant in areas with vegetation, while P_s and P_d are stronger in areas with vertical planes such as buildings.

Figures 5 and 6 show G4U scattering power decomposition images before and after calibration. The images are created by $[R,G,B] = [P_d + \frac{1}{2}P_c, P_v + \frac{1}{2}P_c, P_s]$. In the pre-calibration image, the mountains show a color change correlated with elevation, and some cropland shows red, indicating P_d. On the other hand, in the post-calibration image, woods in mountain and cropland appear green and buildings appear purple, as expected. This shows that the calibration is working well.

5 Conclusions

In this study, we calibrated the Pi-SAR2 polarimetric observation data by sorting out the sources of error and correcting each of them. We also validated the calibration results by performing scattering power decomposition. We applied these processes to approximately 125 TB of observation data in 7266 scenes using computational resources of the ABCI. In the future, we would like to make color images of all calibrated data and post them on the Web so that everyone can see the high-resolution, valuable data. This article is based on a study first reported in the "Construction of a Database of Pi-SAR2 Observation Data by Calibration and Scattering Power Decomposition Using the ABCI" [6].

Acknowledgements

This article is based on results obtained from a project, JPNP20006, commissioned by the New Energy and Industrial Technology Development Organization (NEDO). The authors would like to thank the National Institute of Information and Communications Technology for providing the Pi-SAR2 polarimetric observation data.

References

[1] A. Nadai et al., "Development of X-band airborne polarimetric and interferometric SAR with sub-meter spatial resolution," IEEE IGARSS 2009, Cape Town, South Africa, July 2009; Volume 2, pp. II-913–II-916.

[2] ABCI AI Bridging Cloud Infrastructure. Available online: `https://abci.ai/` (accessed on 5 December 2022).

[3] T. Moriyama, and M. Satake, "Compensation of phase error caused by ground height among polarimetric channels in Pi-SAR-X2," *IEICE Electron. Express* **2014**, *11*, 20140839.

[4] S. Quegan, "A Unified Algorithm for Phase and Cross-Talk Calibration of Polarimetric Data—Theory and Observations," *IEEE Trans. Geosci. Remote Sens.* **1994**, *32*, 89–99.

[5] G. Singh, et al., "General four-component scattering power decomposition with unitary transformation of coherency matrix," *IEEE Trans. Geosci. Remote Sens.* **2012**, *51*, 3014–3022.

[6] Y. Arima et al. "Construction of a Database of Pi-SAR2 Observation Data by Calibration and Scattering Power Decomposition Using the ABCI," *Remote Sensing* **2023**, *15.3*, 849.